

# Soft X-ray spectro-tomography study of cyanobacterial biomineral nucleation

M. OBST,<sup>1,2</sup> J. WANG<sup>2</sup> AND A. P. HITCHCOCK<sup>2</sup>

<sup>1</sup>Center for Applied Geoscience, Tuebingen University, Tuebingen, Germany

<sup>2</sup>Brockhouse Institute for Materials Research, McMaster University, Hamilton, ON, Canada

## ABSTRACT

Quantitative three-dimensional (3D) chemical mapping using angle-scan spectro-tomography in a scanning transmission (soft) X-ray microscope (STXM) has been used for the first time to characterize the early stages of CaCO<sub>3</sub> biomineral nucleation on the surface of planktonic freshwater cyanobacterial cells of the strain *Synechococcus leopoliensis* PCC 7942. The apparatus for STXM angle-scan tomography is described. Aspects of sample preparation, sample mounting and data acquisition and quantitative analysis and interpretation are discussed in detail. Angle-scan tomography and chemically selective 3D imaging at multiple photon energies has been combined with a complete 2D spectromicroscopic characterization of the biochemical and mineralogical composition. This has provided detailed insights into the mechanisms of mineral nucleation, leading to development of a detailed model of CaCO<sub>3</sub> nucleation by the cyanobacterial strain *S. leopoliensis* PCC 7942. It shows that Ca is absorbed by the extracellular polymeric substances (EPS) of the cyanobacteria and that CaCO<sub>3</sub> with aragonite-like short-range order is precipitated rather homogeneously within the EPS. The precipitation of the thermodynamically more stable calcite polymorph then starts at Ca-rich hot spots within the EPS and close to the cyanobacteria.

Received 22 May 2009; accepted 25 September 2009

Corresponding author: M. Obst. Tel.: +49 - (0)7071 29 74701; fax: +49 - (0)7071 29 5059; e-mail: martin.obst@uni-tuebingen.de

## INTRODUCTION

Bacteria, bacterial consortia and biofilms are often associated with metal ions and minerals in natural environments. However, it is often difficult to characterize their role in metal adsorption and biomineral nucleation. Conventional and advanced electron microscopy techniques such as transmission electron microscopy (TEM) (e.g. Konhauser, 1997; Phoenix *et al.*, 2000; Daulton *et al.*, 2001; Benzerara *et al.*, 2005) or scanning electron microscopy (SEM) (Schadler *et al.*, 2008 and references therein) are meanwhile well established amongst the geomicrobiological community. Synchrotron-based techniques such as scanning transmission X-ray microscopy are recently attracting more and more interest. Soft X-ray STXM (100–2500 eV) combines high spatial resolution (~25 nm) with the chemical sensitivity of near-edge X-ray absorption fine structure (NEXAFS) spectroscopy (Bluhm *et al.*, 2006). This is advantageous over the conventional techniques since STXM not only allows characterization of the elemental composition of adsorbates and minerals, but also speciation of sorbed metals and (bio)minerals and character-

ization of the organochemical composition of the bacterial/biofilm components associated with the metals or minerals (Lawrence *et al.*, 2003; Benzerara *et al.*, 2004a,b; Dynes *et al.*, 2006b; Hunter *et al.*, 2008).

Until recently, soft X-ray spectromicroscopic data sets were most often acquired, analyzed and presented as 2D projections of samples which in reality have three dimensions. This is possible as the typical thickness of biogeochemical samples used in STXM (0.5–1 µm) is about the same as the depth of focus (0.5–2 µm) of the most commonly used zone plate focusing optics. However, often complex biogeochemical samples consist of a 3D structure of micro-organisms which are embedded in a matrix of EPS. Analyzing only 2D projections of these 3D structures can hide important details about the spatial arrangement of metals or minerals and the association of those with different components of biofilms or micro-organisms. This issue is particularly relevant when studying mechanisms of mineral precipitation, where it is important to know whether the nucleation and precipitation is mediated inside the micro-organisms, in the periplasm (Miot *et al.*, 2009) or within the EPS surrounding the cells (Obst *et al.*,

2009a). Sometimes this question can be addressed by correlative microscopies (Lawrence *et al.*, 2003) or by analyzing ultrathin sections in the TEM, as shown by Miot *et al.* (2009). In this study we present and discuss a new approach that combines speciation sensitivity, and high spatial resolution in 3D and therefore has a very high potential to address geomicrobiological questions. We present the first results of STXM-based angle-scan tomography of single cyanobacterial cells precipitating CaCO<sub>3</sub>. Cyanobacteria are known to play an important role in the process of CaCO<sub>3</sub> precipitation and *Synechococcus* strains were observed to be responsible for the precipitation of calcite on large scales (Thompson *et al.*, 1997). Different active and passive mechanisms of nucleation were observed under different environmental conditions such as chemical changes in the diffusion-limited microenvironment of cyanobacteria in microbial mats caused by photosynthetic uptake of inorganic carbon (e.g. Merz-Preiss, 2000) or the nucleation of calcite crystals on a proteinaceous surface layer (S-layer) of cyanobacteria (Schultze-Lam *et al.*, 1992). S-layers were observed for several cyanobacterial strains but have not been reported so far for *Synechococcus leopoliensis* PCC 7942. Recently, an amorphous CaCO<sub>3</sub> phase with aragonite-like short-range order (aragonite-like CaCO<sub>3</sub>) has been found as a transient precursor phase of calcite precipitation by freshwater cyanobacteria of the strain *S. leopoliensis* PCC 7942 (Obst *et al.*, 2009a). The authors identified the aragonite-like phase in projection image sequences across the Ca-2p absorption edge of whole, air-dried *S. leopoliensis*. This metastable phase, however, has never been observed in TEM images acquired after conventional TEM sample preparation such as high pressure freezing followed by freeze substitution, embedding in resin, heavy metal staining and ultramicrotomy. Thus, the precise localization of the different Ca phases with respect to the cyanobacterial cell and the surrounding extracellular polymers has remained a challenge. In this study we use a combination of the previously mentioned 2D spectromicroscopy approach and 3D STXM angle-scan tomography to 3D map and co-localize the involved biomacromolecules and Ca species at high spatial resolution.

## METHODS

### Tomography sample holder

Based on the design described by Johansson *et al.* (2007), a tomography sample holder was developed which allows rotating a stripe of a conventional 300 mesh copper TEM grid which is only a single square wide (~120 µm) in the focal point of a STXM. This sample holder was used to acquire angle-scan tomography data sets of single cyanobacteria attached to a lacey carbon-coated grid, over an angle range of ±70° relative to the photon beam axis. The set-up is depicted in Fig. 1. The 0.9-mm diameter rod to which the grid section was glued, was rotated by a two-phase micro-stepper motor with a 1 : 64

gearbox and an optical rotary encoder as described elsewhere (Johansson *et al.*, 2007). The motor/gearbox combination was mounted onto a standard aluminium STXM sample plate. For geometric reasons, we used cells close to the centre of the TEM grid square for angle-scan tomography, which allowed us to cover an angle range of ±70°. For 2D spectromicroscopic studies we used cells close to the edges of grid squares where the grid bars limit the angle range.

### Cell culture

All solutions used in these experiments were prepared from reagent grade chemicals (Sigma-Aldrich Canada Ltd, Oakville, ON, Canada) and millipore deionized water. Planktonic cyanobacteria of the strain *S. leopoliensis* PCC 7942 were cultured in relatively nutrient-poor Z/10 medium for 25 days as described in detail elsewhere (Obst *et al.*, 2009a). The cells were harvested by filtration and re-suspended in 1.4 mM NaHCO<sub>3</sub> solution.

### Sample preparation

CaCl<sub>2</sub> was added to the cell suspension to reach a final concentration of 2.9 mM (six times saturated with respect to calcite) as described in detail elsewhere (Obst *et al.*, 2009a). Lacey carbon-coated 300-mesh Cu grids were dipped into the cell suspension and the water was removed completely from beneath using a filter paper in order to prevent artificial precipitation from drying. The grid was prescreened under an optical microscope and a grid-stripe with sufficiently high numbers of attached cells was selected. These stripes were carefully cut, and then centred, aligned and glued onto 0.9-mm Ø stainless steel rods which were flattened at 1/2 of the diameter for a length of 1 mm on one side (Fig. 1B).

### Scanning transmission X-ray microscopy data acquisition and analysis

X-ray spectromicroscopy was carried using the STXMs of the beamlines 5.3.2 (Kilcoyne *et al.*, 2003) and 11.0.2 (Bluhm *et al.*, 2006) of the Advanced Light Source (ALS). The beamlines were operated at a energy resolving power  $E/\Delta E \geq 3000$ . The energy scale was calibrated by measuring CO<sub>2</sub> and N<sub>2</sub> gas spectra prior to or after the measurements. The main Ca-2p<sub>1/2</sub> → 3d resonance peak in all forms of Ca observed in this work was found to occur at 352.6 eV, consistent with previous studies (Benzerara *et al.*, 2004b). All images were converted to linear absorbance (optical density, OD) scale where

$$OD = -\ln(I/I_0^{-1}),$$

$I$  is the intensity at any pixel on the sample and  $I_0$  is the incident intensity measured in an empty area adjacent to the sample.

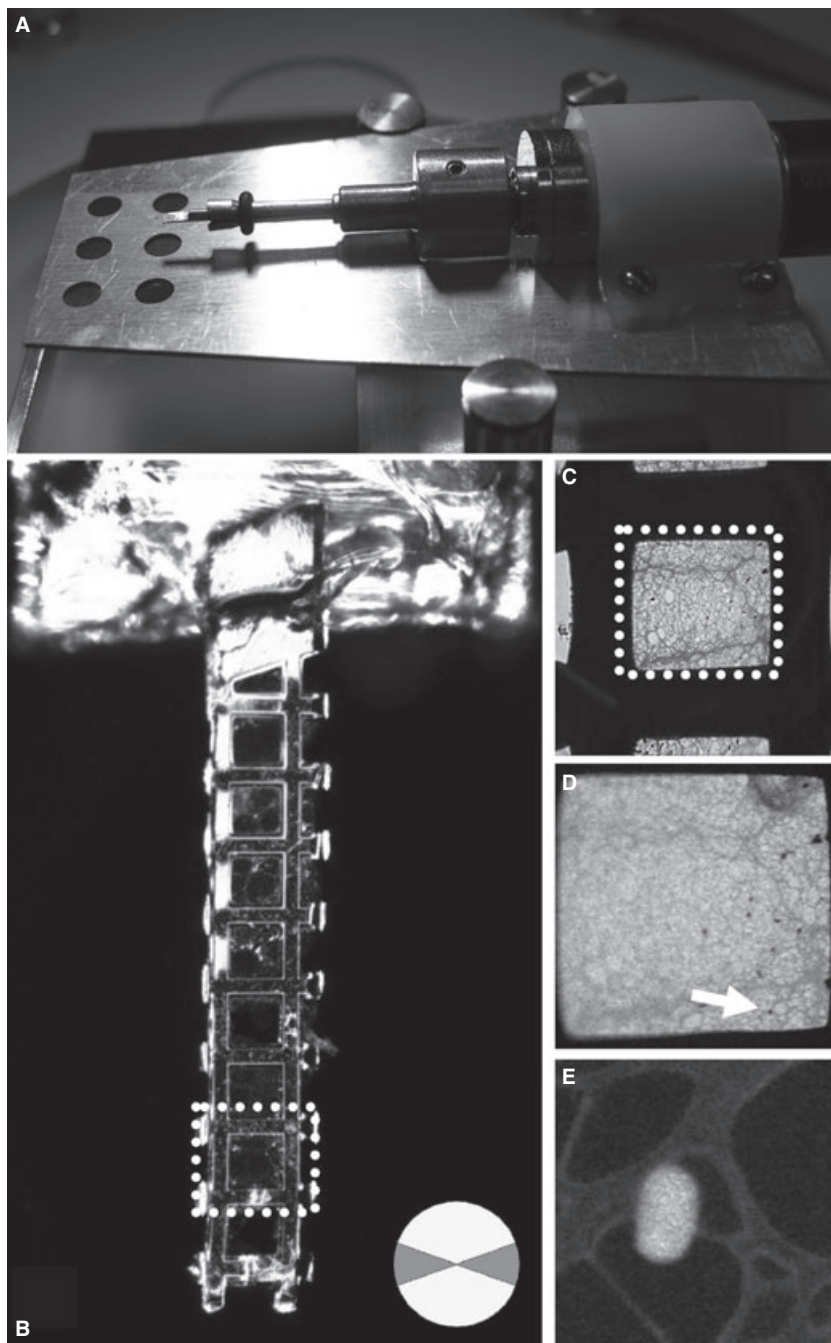


**Fig. 1** (A) STXM tomography apparatus allowing the rotation of a sample in the beam path of a scanning transmission X-ray microscope. (B) Lacey carbon-coated TEM grid stripe glued on a stainless steel rod adaptor and aligned carefully under an optical microscope. The possible angle range, limited by the thickness of the grid bars, is indicated by the inset in (B). Resulting reconstruction artefacts from the 'missing wedge' can be reduced by iterative reconstruction methods. The selected grid square is marked by a dotted line and presented at higher magnification in (C), showing individual cyanobacteria on the lacey carbon support. (D) STXM image of the same section in transmission scale taken at 288.2 eV. The arrow indicates a single bacterium which was selected for a detailed 2D spectro-microscopic characterization (see Fig. 2). (E) X-ray absorption image on optical density (OD) scale of this bacterium at 288.2 eV.

### Spectroscopy

For the spectromicroscopic characterization, image sequences (stacks) were recorded at the C-1s (282–310 eV) and Ca-2p (340–360 eV) edges, with a spectral sampling of 100 meV (C-1s) and 80 meV (Ca-2p) in the spectral regions of interest. The spatial sampling of the images was 25 nm. Images and image sequences were analyzed using the aXis2000 software package (Hitchcock, 2008). The image sequences were aligned and converted to OD. According to Lambert–Beer's

law, OD is directly proportional to the amount of the individual compound in the X-ray beam path. Quantitative composition maps were obtained by singular value decomposition (SVD, Koprinarov *et al.*, 2002) of the C-1s image sequences using previously recorded reference spectra for protein, polysaccharides, lipids, carbonate and the signal of H<sub>2</sub>O which has no spectral features at the C-1s and Ca-2p edges. All reference spectra (for C-1s reference compounds and spectra thereof, see Dynes *et al.*, 2006a; for Ca-2p reference compounds and spectra thereof, see Obst *et al.*, 2009a) were on a linear

absorbance scale (per nm) so the grey scales of each component map, which are constructed from the SVD fit coefficients, give the effective thickness (in nm) of that component at each pixel, assuming that the density is the same as that in the reference compound.

Because of the extremely sharp and intense Ca-2p  $\rightarrow$  3d resonance peaks, it was important to consider potential problems with absorption saturation, which affects quantification and possibly even speciation on account of spectral distortion. Although absorption saturation was not a problem in the data sets of this study, the data sets were treated equally to a previous study (Obst *et al.*, 2009a) for better comparability: the Ca-2p image sequences were analyzed by deleting the images within 0.3 eV of the energies of the two highest resonance peaks (349.3 and 352.6 eV), as described in greater detail elsewhere (Hanhan *et al.*, 2009; Obst *et al.*, 2009a). The image sequences were then decomposed into their principal components using the principal components analysis widget (V1.1) (Lerotic *et al.*, 2004) accessed through aXis2000 (Hitchcock, 2008). Reference spectra of calcite, aragonite, vaterite, Ca-hydroxyapatite, Ca<sup>2+</sup> adsorbed to EPS and a calculated spectrum of organic carbon 'CH<sub>2</sub>O' which has no spectral features at the Ca-2p edge were used as target spectra and fitted with the principal components by minimizing the difference between a linear combination of the principal components and the target spectra. The reference spectra derived in this manner were then used as references for SVD mapping. As described in detail previously (Obst *et al.*, 2009a), vaterite and Ca-hydroxy-apatite were excluded from the final fits because of their spectral differences from the measured data.

### 3D chemical mapping

Species and elemental maps for the organic carbon signal, dominated by protein, and for total Ca, respectively, were derived from the difference of OD images at specific X-ray energies recorded with the sample oriented at 28 different angles ( $\pm 70^\circ$  around the plane perpendicular to the incident photon beam in steps of  $5^\circ$ ). The organic carbon maps are the difference of images recorded at 288.2 and 282 eV. The absorption at 288.2 eV is dominated by the C-1s  $\rightarrow \pi^* \text{C=O}$  transition of protein (Dynes *et al.*, 2006b), but also contains some signal from other major bioorganic macromolecules such as lipids (membranes) and polysaccharides (extracellular polymeric substances, EPS) and minor contributions of carbonates. 282 eV is prior to the onset of C-1s absorption signal. The total calcium maps are from the difference of OD images recorded at 352.6 eV (Ca-2p<sub>1/2</sub>  $\rightarrow$  Ca-3d resonance) and at 350.3 eV (in the dip between the 2p<sub>3/2</sub> and 2p<sub>1/2</sub> resonances).

The resulting organic carbon and Ca maps were pre-aligned for lateral shifts using the ZIMBA algorithm of aXis2000 (Hitchcock, 2008). The final alignment was then performed in a two-step approach using the alignment algorithm in

TOMOJ (Messaoudil *et al.*, 2007): First, the Ca maps were aligned in order to compensate for shifts in X and Y and for small rotation angle deviations around the Y-axis. The organic carbon maps were then aligned with the Ca maps for each individual rotation step. The quality of the alignment turned out to be essential for a good reconstruction. A comparison of the size of small features ( $\sim 80$  nm) between the 2D projection and the 3D reconstruction was used as an indicator for the quality of the alignment and the alignment was only accepted when these features were resolved. The reconstruction was carried out in TOMOJ using a serial iterative reconstruction technique (SIRT) with 200 iterations and a relaxation coefficient of 0.05. Iterative reconstruction techniques such as SIRT (Gilbert, 1972) or algebraic reconstruction techniques (ART) (Herman *et al.*, 1973) are advantageous compared with the conventional back-projection method particularly for reducing artefacts resulting from the missing wedge problem (Midgley & Weyland, 2003).

The reconstructed volume data sets with a voxel size of  $20 \times 20 \times 20 \text{ nm}^3$  were rendered using EM3D (Ress *et al.*, 2004) and VOLUMEJ with Levoy classifier with 0.8% deviation (Abramoff & Viergever, 2002).

### Quantitative analysis of the volume data

In order to analyze the 3D reconstructed volume data sets quantitatively, a calibration of the volume data set was required. Therefore, the volume data set was summed in the Z-dimension which resulted in an artificial projection of the same orientation as the 2D projection maps acquired at  $0^\circ$  angle. The optical density from the direct measurement was then linearly related to the volume data set according to the intensity of the individual voxels that were combined into one pixel in the artificial projection, using the following equation:

$$\text{OD}(x, y)_P = \sum \text{OD}(x, y, z)_T$$

where  $\text{OD}(x, y)_P$  is the optical density of an individual pixel from the species maps ( $0^\circ$  rotation) and  $\text{OD}(x, y, z)_T$  is the optical density of an individual voxel in the tomography 3D reconstructed data set. Precision and accuracy of these methods are discussed later in the manuscript.

## RESULTS

Quantitative maps of the major biochemical macromolecules (Fig. 2A–H) and Ca species (Fig. 2I–O) were derived by SVD of C-1s and the Ca-2p image sequences. The cyanobacterial cell in the centre was mostly composed of protein (Fig. 2A) and lipids (Fig. 2C). Whereas the protein and lipid distributions in the projection maps were rather centred around the cell axis, the distribution of polysaccharide was more spread out, which indicates that the protein-rich cyanobacterial cell is embedded in a thin layer of polysaccharide-rich EPSs

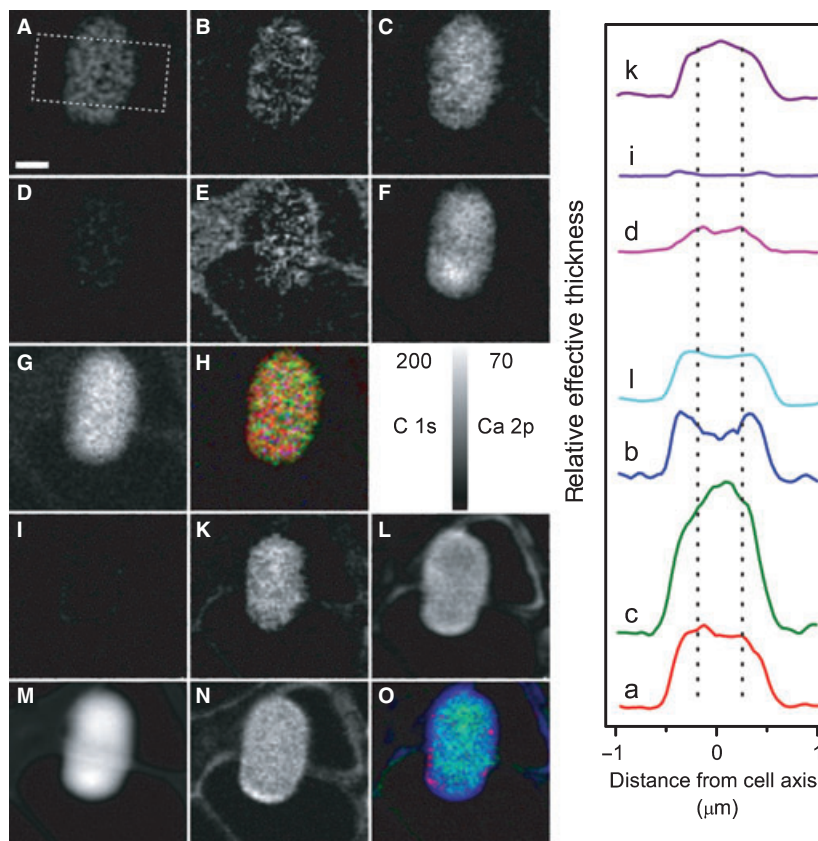


**Fig. 2** Left: speciation maps of a *Synechococcus leopoliensis* cell (scale bar 500 nm). All maps were derived spectro-microscopically from the C-1s (A–H) or the Ca-2p absorption edges (I–O). The species-specific maps are presented on an effective linear thickness scale from 0 (black) to 200 nm (C-1s) or 70 nm (Ca-2p) respectively. The maximum thickness (MT) is listed in nm, scale bar 500 nm. (A) protein map, MT = 105 nm, (B) polysaccharide map, MT = 260 nm, (C) lipid map, MT = 190 nm, (D) carbonate map, MT = 69 nm, (E) lacey carbon map, MT = 200 nm, (F) C-1s non-specific background without spectral features at the C-1s edge, fitted as H<sub>2</sub>O and representing all species that absorb at energies lower than C-1s, (G) standard deviation of the C-1s fit with a maximum (white) of OD 0.1. (H) RGB overlay of C-1s maps of (polysaccharide + lipid) (red), protein (green) and carbonate (blue), each colour scale adjusted individually. (I) Calcite-like CaCO<sub>3</sub> map, MT = 15 nm, (K) aragonite-like CaCO<sub>3</sub> map, MT = 71 nm, (L) adsorbed Ca<sup>2+</sup> map, MT = 62 nm, (M) non-specific Ca-2p background without spectral features at the Ca-2p edge, fitted as organic carbon CH<sub>2</sub>O and representing all species that absorb at energies below the Ca-2p edge. (N) Standard deviation of the Ca-2p fit with a maximum (white) of OD 0.05, (O) RGB overlay of Ca-2p maps of calcite (red), aragonite-like CaCO<sub>3</sub> (green) and adsorbed Ca<sup>2+</sup> (blue), each colour scale adjusted individually. Right: average cross-section profiles of the individual carbon and calcium species across the cyanobacterial cell, perpendicular to the length axis of the cell as indicated by the box in (A). All profiles are presented on the same relative effective thickness scale; the labels of the profiles correspond to the maps presented on the left-hand side.

(Fig. 2B, consider the grey scale as explained in the figure caption). Small amounts of carbonate were also detected in close proximity to the cell (Fig. 2D,H, blue). The area is consistent with the map of aragonite-like CaCO<sub>3</sub> derived from the analysis of the Ca-2p edge (Fig. 2K,O, green), although the effective thickness of the carbonate layer is slightly underestimated comparing the results of the C-1s fit with the result of the Ca-2p fit (see profiles Fig. 2 right). The aragonite-like layer was surrounded by a Ca species with the spectral signature of Ca<sup>2+</sup> adsorbed to EPS. This spatial arrangement resulted in a rim-like distribution in projection (Fig. 2L,O, blue). Only very small amounts of calcite-like CaCO<sub>3</sub> were detected in the periphery of the cell but well within the extracellular polymers (Fig. 2I,O, red). Due to its distinct C-1s spectrum, the lacey carbon support structure

could be mapped and separated from the cell structure (Fig. 2E), although some lacey carbon signal was mapped in the area of the cell as well. Potential reasons for this observation will be discussed later.

Quicker but chemically less specific maps were derived from images taken at specific energies and image difference maps on linear absorbance (OD) scale. Figure 3A displays an OD image at 350.3 eV where the absorption is dominated by C-1s continuum absorption. Thus, Fig. 3A can be interpreted as a non-specific map of the carbon content. The interpretation of such single energy maps requires additional knowledge about the composition of the analyzed sample. Figure 3C presents a more chemically specific OD image constructed from the difference of OD images at 352.6 eV (peak of the Ca-2p<sub>1/2</sub> → 3d resonance, Fig. 3B) and 350.3 eV (Fig. 3A).

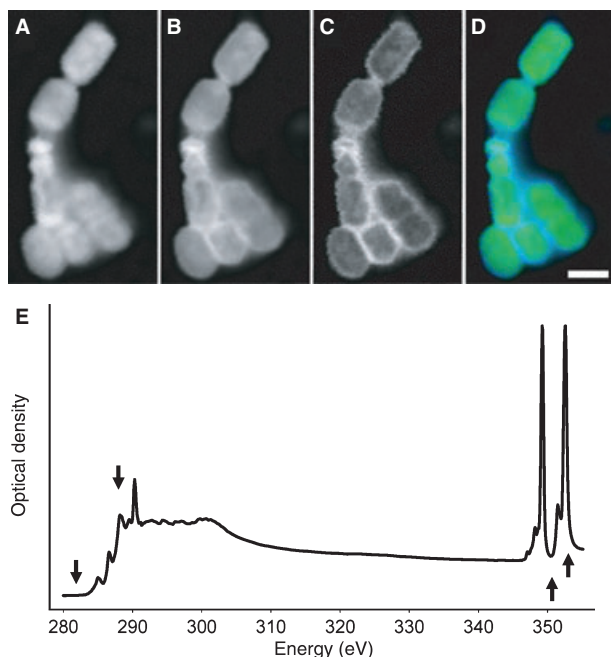


**Fig. 3** (A) OD image at 350.3 eV where the absorption is from the C-1s continuum, and thus it is a map of total carbon. (B) OD image at 352.6 eV where the absorption is common to all relevant Ca species, but still contains contributions from C-1s absorption. (C) Ca map from the difference of 352.6 and 350.3 eV OD images. (D) Colour overlay of (A) (green) and (C) (blue), showing the distribution of Ca around the cyanobacteria. (E) Average absorption spectrum across C-1s and Ca-2p absorption edges of a whole *Synechococcus leopoliensis* cell. The arrows indicate the energies which were used for 3D chemical sensitive mapping in this study. The 288.2–282.0 eV OD image difference represents mainly the organic components of the bacteria and is dominated by the protein, followed by lipids, but also contains minor contributions of the carbonate absorption. The 352.6–350.3 eV OD image difference represents the total Ca content (scale bar 1  $\mu\text{m}$ ).

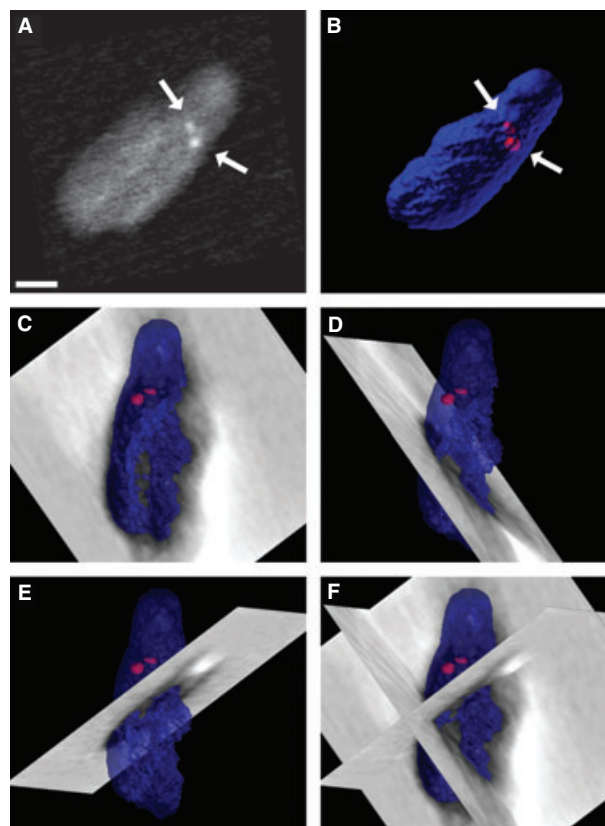
This difference map is specific to the absorption of Ca and represents an elemental map of the total Ca. It does not require additional information for interpretation as all known  $\text{Ca}^{2+}$  species exhibit a strong absorption resonance at 352.6 eV. Although all images presented in Fig. 3 are only 2D projections of a 3D structure, it is obvious that the Ca is located in the periphery of the cell. This becomes even more apparent in the colour overlay (Fig. 3D) wherein the carbon map is presented in green and the Ca map is presented in blue.

Figure 3E shows the average spectrum of a whole cell including the attached EPS layer across the C-1s and Ca-2p edges. The arrows indicate the energies which were selected for chemically specific image difference mapping of the organic carbon compounds ( $\text{OD}_{288.2\text{eV}} - \text{OD}_{282.0\text{eV}}$ ) and Ca ( $\text{OD}_{352.6\text{eV}} - \text{OD}_{350.3\text{eV}}$ ). Although the chemical specificity is not as good as a spectral fit using SVD of a full image stack with extensive sampling in spectral space, the organic carbon maps are found to match most closely the protein component maps derived from SVD of a full spectral sampling. The Ca map represents all Ca species present in the sample. A more

detailed interpretation requires further knowledge about the speciation. Therefore, in an ideal case, a 3D chemical sensitive tomography study should be combined with a full 2D spectromicroscopic characterization of the same or a similar sample.

The aligned  $\pm 70^\circ$  rotation series of the OD organic carbon and Ca maps, respectively, is presented in Fig. S1. These species maps were used as the input data for the 3D reconstructions. From the projection images it is apparent that the distribution of the biological macromolecules (i.e. protein) is rather homogeneous compared with the distribution of Ca, which shows higher concentrations in the periphery of the cell including a small protrusion at the upper end of the cell compared with the centre.

Figure 4A shows the Ca projection map at a rotation angle of  $0^\circ$ . The two arrows indicate two hotspots with high Ca



**Fig. 4** (A) Ca map taken at  $0^\circ$  (grid plane perpendicular to beam axis), showing an inhomogeneous distribution with two Ca hot spots indicated by the two arrows ( $\varnothing$  80 and 100 nm). These features could be reproduced in the 3D reconstruction; (B) rendered isosurfaces of Ca representing the sum of Ca (semitransparent blue) and the same hot spots indicated by arrows (red). This indicates that a spatial resolution similar to that achieved in 2D can be achieved in the third dimension, provided the alignment is done carefully and an iterative reconstruction method is chosen to reduce artefacts from the 'missing wedge'. (C–F) Rendered reconstructions (red, blue) overlaid by slice planes in all three directions. The grey scale of the slice planes has been inverted for better visualization (white represents lowest Ca content, black represents highest Ca content) (scale bar 500 nm).

content, one with a diameter of  $\sim 80$  nm, the other one with a diameter of  $\sim 100$  nm. These two features were used to compare the spatial resolution of 2D projections with the spatial resolution of the 3D reconstruction. These two Ca hotspots were only spatially separated and equal in size in the 2D projection and 3D reconstruction when the alignment of individual maps of the angle rotation stacks was done carefully, which in turn was used as an indicator for good alignment. Figure 4B displays the reconstruction at the same orientation with an isosurface rendered equivalent to  $\sim 0.0075$  OD units per nm (blue) and the hot spots rendered equivalent to  $\sim 0.015$  OD units per nm (red). This result clearly indicates that a spatial resolution of better than 80 nm was achieved in the 3D reconstruction. For sufficiently high contrast and sharply defined objects, the intrinsic resolution of a Fresnel zone plate with 25 nm outer zone widths is 30 nm under diffraction limited conditions (Attwood, 2001). A lower

spatial resolution in 3D is to be expected due to the challenges of accurate alignment of the images prior to reconstruction, as well as some reduction due to the missing wedge effect (which is estimated to be very minor in this case – see below). Through the analysis process it was apparent that careful alignment is essential for achieving good spatial resolution in 3D. Figure 4C–F shows grey scale cross-sections through the Ca 3D reconstructed model at different angles illustrating the position of the chosen iso-level (red and blue) for the rendered 3D presentations (NB: For presentation the grey scale of the cross sections is reversed, i.e. showing the highest levels in black and the lowest level in white).

Figure 5 presents a semitransparent RGB overlay of the 3D reconstructed volumes of the Ca hotspots (red), the biological macromolecules (green) and Ca (blue) rendered with VOLUMEJ and displayed from various angles. The cell appears to have a rather smooth flat surface on one side. This

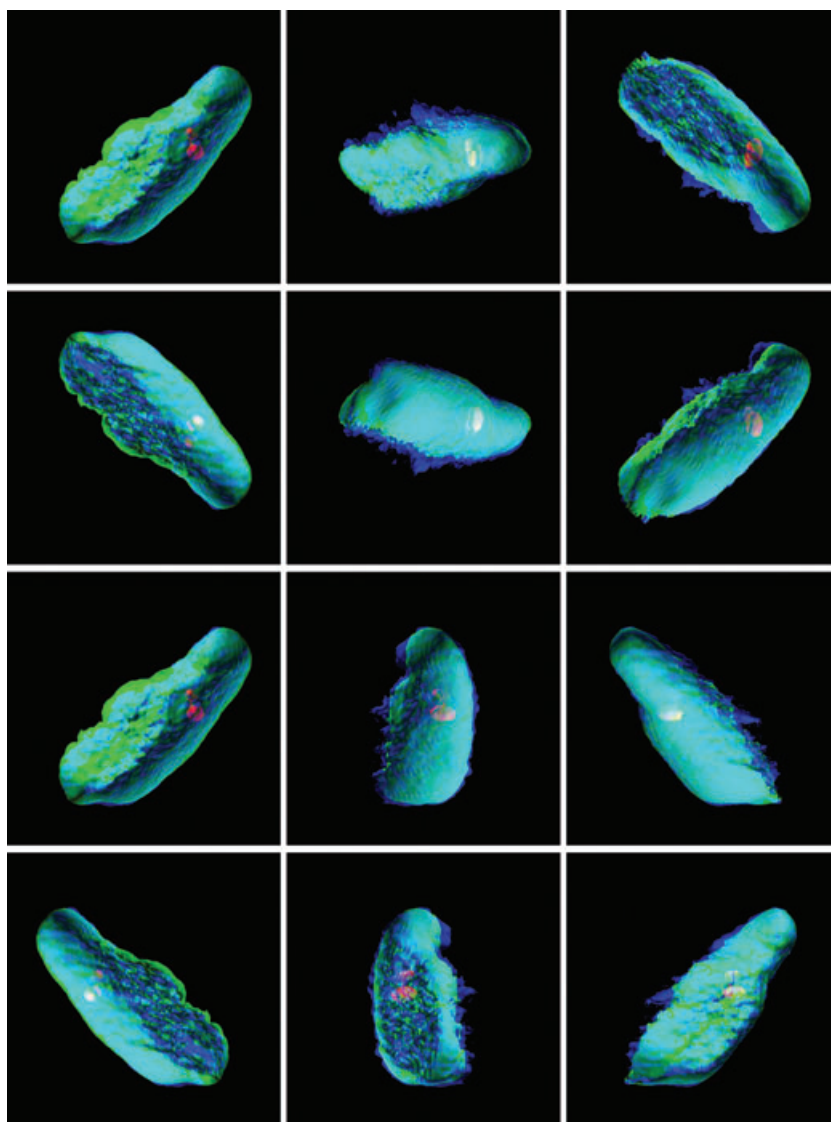


**Fig. 5** Colour overlays of rendered iso-surfaces from various angles; red represents the two Ca hot spots derived from the Ca-2p edge, green represents the organic carbon content derived from the C-1s edge and blue represents the total Ca content, derived from the Ca-2p absorption edge (image size  $3 \times 3 \mu\text{m}^2$ ). Whereas the organic carbon iso-surface looks rather smooth and homogeneous, the Ca iso surface (blue) looks rather rough and partly inhomogeneous.

is the side where the cell was attached to the lacey carbon support structure of the TEM grid. The remainder of the cell surface is quite rough, indicating partial spatial resolution of the EPS adhering to the cell. The iso-level for the organic carbon rendering is equivalent to  $\sim 0.0024$  OD units per nm thickness.

A quantitative analysis of the volume stacks in the spatial domain is presented in Fig. 6A, which shows slices through a volume data set which is the ratio of the 3D Ca maps to the 3D organic carbon maps. The calculations were performed on a voxel-by-voxel basis and the volume was divided into 100 nm thick slices for presentation. Figure 6B–E presents plots of the Ca content versus the organic carbon content in the OD domain over the pixels corresponding to the cell and its surrounding EPS. The 3D data set was manually segmented into three groups. These groups are indicated in red, green and blue in the insert in Fig. 6B, which is a 3D plot in the spatial domain, and by the same colours in the Ca/organic carbon plot in Fig. 6B. The first distinct group of voxels (red) were the two hot spots of Ca which were selected from the Ca maps by thresholding. The Ca/organic carbon contents of this group are plotted in Fig. 6C and shows a very narrow distribution in both organic carbon content and Ca content. The second group was selected in the volume interpreted as ‘cell-internal’ (green in Fig. 3B) excluding the cell membranes and surrounding EPS layers. The distribution of the Ca content of this group (Fig. 6D) is also rather narrow but at a much lower level compared with the hot spots. The distribution of the organic carbon content OD is broader than that of the Ca OD for this group of voxels. The third group of voxels was selected in the volume interpreted as ‘cell envelope’ including the cell membranes and the exopolymers (blue in Fig. 3B). The distributions with respect to both Ca content and organic carbon content are rather broad (Fig. 6E) but can be split into three distinct subgroups of voxels. (I) for low ODs (i.e. concentrations), there is a linear relationship between organic carbon and total Ca with a rather shallow slope. For higher concentrations, there are two subgroups (II) and (III), both with a linear relationship but rather steep slopes of Ca/organic carbon. One is almost vertical (III), which indicates that the amount of Ca is almost independent of the organic carbon content.

## DISCUSSION

### Interpretation of the 3D cyanobacterial $\text{CaCO}_3$ biomineral nucleation study

For the first time STXM angle-scan tomography was used to analyze a geomicrobiological process in three dimensions at a spatial resolution  $<80$  nm, namely biomineralization of  $\text{CaCO}_3$  by cyanobacteria. The microbiological macromolecules of the cyanobacterial cell (combining protein, lipids and polysaccharides), and Ca were mapped and correlated in 3D.

The reconstructed data set could be grouped into sub-volumes of components with different amounts of sorbed Ca. The combination of semi-quantitative image difference mapping with a detailed spectromicroscopic study (Fig. 2; Obst *et al.*, 2009a) allowed a quantitative analysis and interpretation of the resulting volume data sets. The inner part of the cell-mineral aggregate sorbed smaller amounts of Ca, and was interpreted as the cyanobacterial cell, which contains large quantities of protein (Fig. 2; Ingraham *et al.*, 1983). This cell was surrounded by a layer of bio-organic polymers with a relatively higher sorption of Ca (compare Figs 2 and 6A). In a previous, extensive spectromicroscopy study (Obst *et al.*, 2009a), *S. leopoliensis* cells were found to be surrounded by two types of EPS both with a high adsorption capacity for  $\text{Ca}^{2+}$  ions, one closely bound to the cell surface, one more loosely attached. The authors also found an X-ray amorphous  $\text{CaCO}_3$  phase with aragonite-like short-range order which formed within the EPS in an amount that depended on the nutrient concentration during cell culture. The spectroscopic results of this study (not shown) are in keeping with the previously published data. The Ca-rich layer surrounding the relatively Ca-poor cell material was interpreted as EPS containing small amounts of amorphous  $\text{CaCO}_3$  with aragonite-like short-range order (Fig. 2D,K). The last, small and spatially distinct group of voxels (Fig. 4, red) containing large amounts of Ca were interpreted as the nuclei of  $\text{CaCO}_3$  crystals.

The 3D data set was analyzed not only in the spatial domain (Fig. 6A) but also in the compositional domain (species ratios, Fig. 6B). Different groups of organo-chemical compounds with distinct affinities for Ca were easily identified. Therefore, this analysis method provides additional confidence for data interpretation and model development. The potential of the analysis of species ratios becomes most obvious for the rather small and distinct group of voxels of the Ca hot spots which were interpreted as  $\text{CaCO}_3$  (Fig. 6C). Here, one sees clear differences among the biomacromolecules with respect to their Ca sorption. Group I in Fig. 6E with a rather shallow slope of Ca/organic carbon is interpreted as adsorption of Ca to rather weakly sorbing compounds such as proteins and lipids of the cell membranes. Group II was interpreted as Ca adsorption to polysaccharide-rich exopolymers (middle slope) and Group III (steep slope, almost vertical) was interpreted as precipitation of the aragonite-like  $\text{CaCO}_3$  layer which is embedded in exopolymers, where the Ca content is almost independent of the organic C content. This line is steep but not completely vertical as the absorption of carbonate-carbon contributes only a minor fraction of the X-ray absorption at 288.2 eV. The expected relatively lower sorption of Ca by the cell-internal structure which is dominated by protein and lipids could be verified (Fig. 6D). The cell-internal structure appeared to be much more homogeneous regarding the Ca/organic carbon content compared with the ‘cell envelope’, which combines the cell membrane and the EPS (see Fig. 6B).

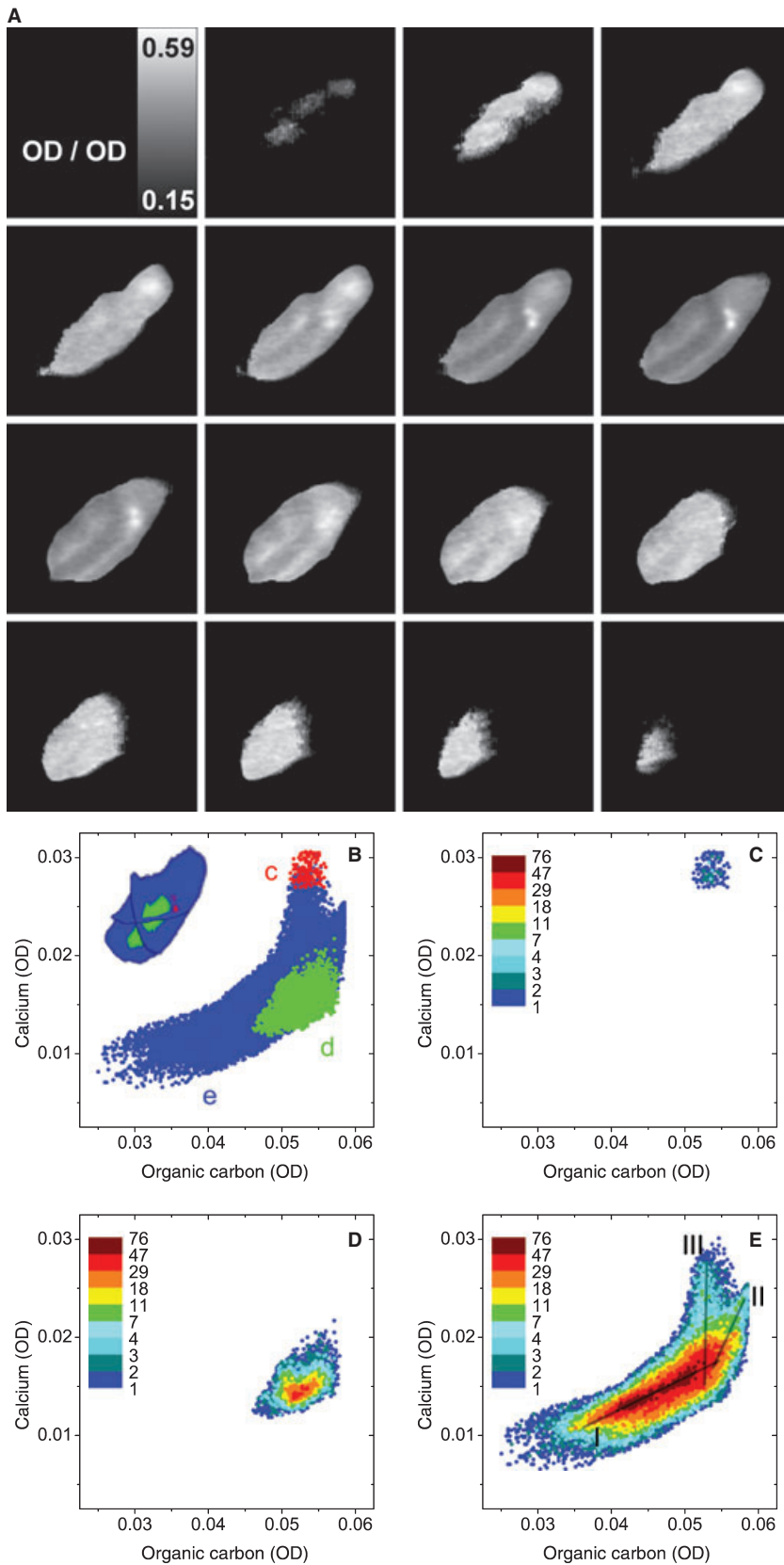


**Fig. 6** (A) Quantitative maps of the Ca/organic carbon absorbance ratio derived from the C-1s and the Ca-2p volume stacks. These volume stacks were separated into 100-nm slices which are presented as a sequence cutting throughout the *Synechococcus leopoliensis* cell. The absorbance ratios are presented as a grey scale (OD/OD) from 0.15 (black) to 0.59 (white) which is equivalent to a mass ratio ( $\text{g g}^{-1}$ ) ranging from 0.03 (black) to 0.13 (white). (B) Correlation plot of the Ca absorbance ( $\text{OD}_{352.6} - \text{OD}_{350.3}$ ) and the organic carbon absorbance ( $\text{OD}_{288.2} - \text{OD}_{282.0}$ ); the 3D data set was segmented manually into the Ca hot spots (red, C), the cell-internal volume (green, D) and the cell envelope including EPS and extracellular precipitates of  $\text{CaCO}_3$  (blue, E) except for the previously mentioned hot spot. The 3D insert in (B) indicates the location of the voxels in within the volume of the cell-mineral aggregate. (C) Correlation plot of the voxels segmented as 'Ca hot spot'. (D) Correlation plot of the voxels segmented as 'cell-internal volume'. (E) Correlation plot of the voxels segmented as 'cell envelope'. The data points in (C–E) are clustered and presented on a logarithmic colour scale. See text for interpretation.

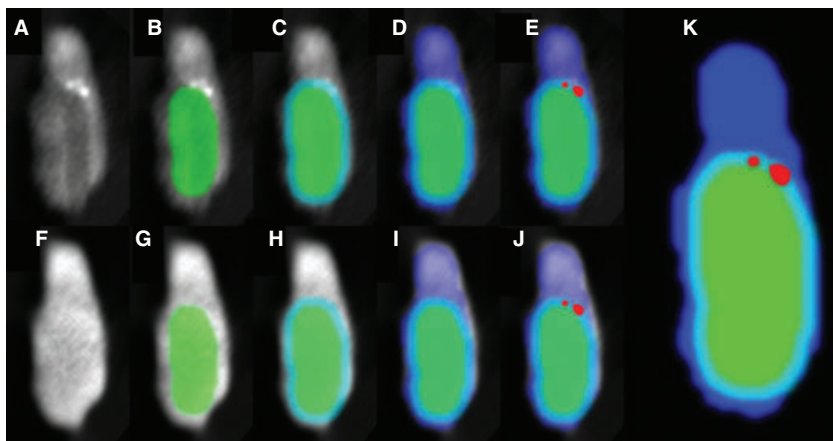


**Fig. 7** Interpretive 3D model (K) of the nucleation of  $\text{CaCO}_3$  biominerals on the surface of *Synechococcus leopoliensis* overlaid on the meridional slice of the cell displaying the Ca content (A) and the organic carbon content (F). The central part (green) indicates the cell (B,G), which is surrounded by a layer of strongly bound EPS (light blue, C,H). This structure is embedded in loosely bound EPS (dark blue, D,I) which adsorb large amounts of  $\text{Ca}^{2+}$ . The hot spots of Ca are most likely  $\text{CaCO}_3$  crystals (red, E,J) which nucleate within the closely bound EPS.

In order to assist interpretation, sections from the 3D data set are displayed in Fig. 7 which shows the central plane of the 3D data set of the organic carbon and the Ca reconstructions overlaid by colour-coded entities of the organochemical and biomineral compounds on the Ca maps (upper row) and the organic carbon maps (lower row). At the meridian of the cell it is surrounded by extracellular polymers. These were subdivided into: (i) closely bound polymers which are strongly attached to the cell surface and (ii) loosely bound polymers which can be sheared off (Obst *et al.*, 2009a). These loosely bound polymers were partially sheared off the analyzed cell and formed a bead attached to one end of the cell. It is unclear whether this is an artefact from sample preparation. However, the preparation was done very carefully and involved only one filtration step, but no centrifugation prior to the incubation in the supersaturated  $\text{NaHCO}_3/\text{CaCl}_2$  solution. The hotspots of Ca, which were interpreted as  $\text{CaCO}_3$  nuclei, formed externally to the cell but in close proximity to the outer cell membrane and close to one of the poles of the rod-shaped cyanobacterial cell. This interpretation is based on both the 3D data set and the results of the detailed spectromicroscopic analysis of the *S. leopoliensis* cell presented in Fig. 2, wherein the highest concentrations of hot spots of calcite were also found to be located outside the cell but close to the cell membrane (Fig. 2E right). At this point it remains unclear whether the nucleation of the calcite is directly related to membrane bound cell surface proteins. However, Umeda *et al.* (1996) identified membrane-bound proteins in PCC 7942 which were similar to bacterial S-layer proteins, and cyanobacterial S-layers of different strains have been reported to be able to mediate calcite nucleation (Schultze-Lam *et al.*, 1992).

The interpretation of this data set emphasizes the complementarity of 2D and 3D STXM studies. Whereas the 2D studies allowed for the spectroscopic identification and the specific spectromicroscopic 2D mapping of chemical species, the 3D studies focused on 3D mapping but with lower specificity. The grouping and identification of the individual biomacromolecules using co-localization analysis was only possible in

the reconstructed 3D data set as the individual compounds overlap in 2D projections of the rod-shaped cells which are surrounded by exopolymers. The individual biomacromolecules and Ca species, which were identified in a previous 2D spectromicroscopic study (Obst *et al.*, 2009a), were co-localized in 3D in the present study and could clearly be differentiated with regard to their Ca/organic carbon ratio. This ratio was used to verify the association of the aragonite-like  $\text{CaCO}_3$  layer with the EPS layer surrounding the cells. The hot spots of Ca which were interpreted as calcite nuclei appeared in the direct extension of the almost vertical line in the Ca/organic carbon plot (III) in Fig. 6E, indicating that the calcite nuclei have a relatively higher Ca content per amount of organic carbon. A potential explanation for this relatively higher content could be that the amorphous aragonite-like  $\text{CaCO}_3$  layer precipitates within an organic framework of EPS which in turn might limit the crystal size and cause the layer to be X-ray and electron-amorphous (Obst *et al.*, 2009a). By contrast, the calcite nuclei seem to exclude the polymers from the crystal structure and therefore have a higher density. The limitation of the Ca content of the aragonite-like  $\text{CaCO}_3$  layer surrounding the bacteria (group III in Fig. 6E) in comparison with the calcite nuclei (Fig. 6C) can be interpreted as another indication that the amorphous aragonite-like  $\text{CaCO}_3$  layer is the result of protection mechanisms of the cyanobacteria against the uncontrolled precipitation of the thermodynamically stable calcite on their surface (Obst *et al.*, 2009a). This is in keeping with the conclusion of the previous study on  $\text{CaCO}_3$  nucleation by cyanobacteria, namely that the nucleation is a three-step process wherein first  $\text{Ca}^{2+}$  is adsorbed to the EPS, followed by the precipitation of an amorphous  $\text{CaCO}_3$  layer with aragonite-like short-range order. The aragonite-like layer was found to be a transient precursor phase of calcite precipitation, which is the final and thermodynamically stable  $\text{CaCO}_3$  phase in this system. At this stage it is unclear but unlikely that the observed calcite nuclei would have resulted in the precipitation of micron-sized calcite crystals, which were normally only found to precipitate on a rather small

fraction of the *S. leopoliensis* cultures (Obst *et al.*, 2009b). Similar precipitation mechanisms, which involve cation adsorption and nucleation of a mineral phase within the EPS layer or directly on the cell surface followed by a second stage of precipitation, have been reported previously by Schultze-Lam & Beveridge (1994) for cyanobacterial CaCO<sub>3</sub> nucleation and also for the formation of Fe minerals by bacteria (Konhauser, 1998).

In our previous systematic study of the influence of the EPS layer on the nucleation of CaCO<sub>3</sub> on the surface of *S. leopoliensis*, calcite nucleation was not observed at the times of sampling (Obst *et al.*, 2009a). In the present 2D study (Fig. 2) the amounts of precipitated calcite were also extremely small with a maximum thickness of 15 nm, which is within or below the size range of critical nuclei (De Yoreo & Vekilov, 2003). This indicates that the precipitation of calcite was just starting at the sampling time. These hot spots were located close to one of the poles of the cell (Fig. 2I). Interestingly, the concentration of the adsorbed Ca<sup>2+</sup> species was also higher in the pole regions (Fig. 2L). Although these results are consistent, from this study there is no statistical proof that this phenomenon is common. Nevertheless, we found the observation important enough to discuss it in the context of related examples that have been discussed in the literature. One of the processes which might eventually play a role could be related to cell aging resulting in the accumulation of aggregates of misfolded proteins in the periplasm in pole regions of bacteria. This was found to be potentially related to a preferential Fe encrustation of pole regions of Fe-oxidizing bacteria (Miot *et al.*, 2009). Another mechanism which is not directly transferable as it was observed for Gram-positive bacteria, but still might be related to the observed phenomenon, is the relative accumulation of negative surface charges around bacterial cell poles (Sonnenfeld *et al.*, 1985; Graham & Beveridge, 1994).

#### Potential and limitations of scanning transmission X-ray microscope tomography in biogeosciences

Scanning transmission (soft) X-ray microscopy angle-scan tomography, in combination with a 2D spectromicroscopic characterization, is a state-of-the-art high-spatial resolution technique that allows for chemical species-specific mapping and thus offers new insights into a variety of processes that are relevant in geomicrobiology. The speciation sensitivity of soft X-ray spectromicroscopy which is based on NEXAFS spectroscopy allows for the determination and quantification and mapping of both organic and inorganic chemical species such as biomacromolecules (e.g. protein, polysaccharides, lipids, Dynes *et al.*, 2006b), redox species [e.g. Fe(II)/Fe(III), Miot *et al.*, 2009; As(III)/As(V), Benzerara *et al.*, 2008] or different mineral phases of the same chemical composition (e.g. calcite, aragonite, vaterite, all CaCO<sub>3</sub>, Benzerara *et al.*, 2004b; Obst *et al.*, 2009a) at a spatial resolution of ~25 nm (in the case of the 2D microscopy) or ≤80 nm in the case of the 3D

tomography approach. The possibility of high spatial resolution mapping of different chemical species provides valuable information on spatial arrangement and correlation of the species and allows for interpretations on mechanistic details of geomicrobiological processes such as the sorption of trace metals in dependence on their redox state, biomineral nucleation and mineral transformation reactions in contact or within microbial cells or within biofilms. However, there are several limitations of synchrotron-based 3D spectromicroscopy which are explained in the following paragraphs using this study as an example.

The complete spectromicroscopic characterization with extensive sampling in spectral space at both the C-1s and Ca-2p edges and spatial sampling of 25 nm within a region of 3 × 3 μm<sup>2</sup> took several hours of beam time, and about 6 h of clock time. As the beam time available at synchrotron-based STXM beamlines is very limited, it was necessary to find a compromise between chemical specificity and time efficiency. Further improvements of the data acquisition procedure are needed, in particular automation of location, focusing and framing at successive angles, and ideally a eucentric mounting system which minimizes the lateral motion of the region of interest over the whole 180° angular range.

The excellent control of the photon energy in STXM beamlines and the high-energy resolution allows for fine control of the specificity of chemical mapping. In principle, there are three different methods of mapping, which, depending on the analyzed chemical species and the composition of the sample, vary from close to 100% quantitative compound specificity to rather general, semi-quantitative elemental maps. The first, simplest and least specific approach is imaging at single, selected energies. If the energy of a resonance excitation is selected, the absorption in most cases is dominated by the species or element responsible for this resonance. However, the signal might contain contributions of other species which also absorb at the energy, or even different elements absorbing away from their edge. In this study, 352.6 eV represents such an energy. At this energy, the signal is dominated by the sharp and strong absorption peak of the Ca-2p-L<sub>3</sub> transition (Fig. 3B) but still contains a significant contribution of C-1s absorption. This becomes most obvious when this most simple method of mapping is directly compared with the second, more specific mapping approach which subtracts the pre-edge absorption from the on-resonance image (Fig. 3C). The OD in Fig. 3C is solely related to the absorbance of calcium. In this case, the energy used is common to all major Ca-containing components in the system, calcite, aragonite-like CaCO<sub>3</sub> and Ca<sup>2+</sup> adsorbed to EPS (Obst *et al.*, 2009a). Thus, using differences of OD images does not allow for differentiating between the three species (except for the segmentation approach described above) but does allow for efficient, nearly quantitative mapping of the total Ca content. The specificity in this approach is therefore related to the specificity of the resonance energy that is chosen and on the off-resonance

absorption of other species at this energy. The most specific STXM species mapping approach requires full spectromicroscopic characterization which results in a data set that contains a NEXAFS spectrum at each single pixel of the analyzed area. This data set is obtained by collecting individual images at each photon energy. The resulting spectra of each pixel are then approximated by a linear combination of absorption spectra of reference compounds (Dynes *et al.*, 2006b; Obst *et al.*, 2009a), or the spectra of the individual compounds of the sample are derived internally from statistical methods such as principal components analysis in combination with cluster analysis. In either procedure the sample area can then be mapped quantitatively on a pixel-by-pixel basis with a statistical error in the range of a few percent (Dynes *et al.*, 2006b).

In this 3D tomography study, image difference maps were chosen as a medium specific but still reasonably fast approach to characterize the sample in 3D. The photon energies were chosen to allow selective mapping of the organic carbon components and of Ca. However, in order to optimize the experiment in terms of an efficient use of synchrotron beam time while gaining the maximum information content in the 3D data set, we combined the 3D chemical mapping using STXM angle-scan tomography with a detailed spectromicroscopic characterization of the samples in 2D. This also enabled us to compare the present 3D results with the data from previous experiments. The mechanisms of CaCO<sub>3</sub> biomineralization by *S. leopoliensis* PCC 7942 have been investigated using STXM previously, with a focus on the influence of nutrient conditions, which have been found to influence amount and properties of the EPS produced by this cyanobacterial strain (Obst *et al.*, 2009a). The results of the 2D spectromicroscopic analysis of the samples (Fig. 2) are consistent with the previous study which was carried out in a similar manner except that the sample substrate was Si<sub>3</sub>N<sub>4</sub> rather than lacey carbon-coated TEM grids.

A potential problem and limitation in 3D chemical mapping with STXM tomography is radiation damage. A complete spectromicroscopic characterization requires acquisition of a full image sequence, ideally with 50–100 energies. It is possible to make a few such measurements of a given region using currently typical acquisition parameters (dwell times of ~1 ms per pixel, and a flux of 10<sup>7</sup> photons per second in a 30-nm spot) with negligible radiation damage. However, when this is extended to 20 or more sets of such image sequences, which are needed to cover the angle space adequately, there are major concerns about radiation damage. Clearly, the image difference mapping used in this work is preferable to full image sequences from this point of view. In order to characterize the radiation damage caused by the measurements used in this study, after each image stack acquisition an additional image was taken at an energy of 289 eV, an energy which is sensitive to damage to polysaccharides, the macromolecules which are most easily damaged (Dynes *et al.*, 2006a). Whereas the radiation damage after a single image

stack is only a few percent, multiple complete stacks cause rather significant damage. Thus, a full spectral characterization may not be the most desirable method for angle-scan tomography, which requires 28–180 angles in order to cover 140°–180° of angle range with steps of 5° to 1°. Instead, OD image difference mapping for the angle-scan tomography in combination with a full 2D spectromicroscopical characterization on the same sample prior to the tomographic acquisition (or on a separate sample) appears to be a very good compromise between specificity and radiation damage.

Two other approaches which allow for acquiring high-resolution data in 3D are full-field transmission X-ray microscopy (TXM) and TEM-based tomography. Several synchrotron beamlines dedicated to soft X-ray TXM tomography now exist and TEM tomography in modern instruments can be almost fully automated, which gives both of these techniques significant speed and thus throughput advantages relative to STXM tomography. Particularly if no chemical speciation mapping is required, TXM- and TEM-based tomography are the techniques of choice. However, radiation damage is an important limitation in 3D angle-scan tomography for full-field TXM tomography and TEM tomography. STXM has the advantage that all photons that are transmitted through the sample contribute to the information content of the resulting data set. In a full-field X-ray microscope a post-specimen Fresnel zone plate is used as an objective lens, which reduces the fraction of photons contributing to the information content by approximately an order of magnitude due to the limited zone plate efficiency. Thus, on a per-image basis, TXM is significantly more damaging than STXM. In the so-called water window (between the C-1s and the O-1s absorption edges) STXM also has major advantages compared with TEM combined with electron energy loss spectroscopy (EELS) as the radiation damage necessary to extract the same information content is about an order of magnitude lower for STXM compared with TEM–EELS (Rightor *et al.*, 1997, Hitchcock *et al.*, 2008). Another difference between STXM-, TXM- and TEM-based tomography is sample preparation. TEM requires the sample to be compatible with high vacuum but allows for analyzing cryo-samples. By contrast, in TXM- and STXM-based tomography, the sample can be analyzed in the hydrated state. Dedicated holders for STXM tomography of wet samples are currently under development.

### Quantification

The accuracy of speciation by image differences is dependent on the energies chosen and the sample composition. Therefore, the origin of the absorption contrast at any specific energy has to be considered carefully for each individual experiment. For an average organo-chemical composition of the cyanobacterial cell shown in Fig. 2 (i.e. 26% protein, 44%

lipid, 7% polysaccharide), the contributions to the absorption at 288.2 eV are the following: protein 40%, lipid 34%, lacey carbon 17%, polysaccharide 6% and carbonate 4%. The cell that was analyzed by angle-scan tomography was not placed on but only attached at the side of a piece of lacey carbon. Thus, for the interpretation of the 3D data set the lacey carbon was not considered, which shifts the relative contributions to 48% protein, 41% lipid, 7% polysaccharide and 4% carbonate. The image difference maps of  $OD_{288.2\text{eV}}-OD_{282\text{eV}}$  which we label as organic carbon maps are actually mapping all of the cell (protein and lipids) and some of the extracellular polymers (lipids and polysaccharides). As discussed previously, the image difference  $OD_{352.6\text{eV}}-OD_{350.3\text{eV}}$  is common for all Ca species. Therefore, the Ca maps represent the distribution of total calcium.

### Quantification errors and limits associated with reconstruction

Although soft X-ray spectromicroscopy in transmission mode is a quantitative technique (Bluhm *et al.*, 2006) as the NEXAFS absorption contrast correlated with the amount of the species in the beam path by the Lambert–Beer law, several limitations and potential sources of errors and artefacts have to be considered. The most accurate quantification method based on spectral deconvolution techniques (e.g. the fits presented in Fig. 2) results in statistical errors as low as a few percent (Dynes *et al.*, 2006b). However, care has to be taken as this method can result in systematic errors if the selection of reference spectra is inappropriate for the analyzed samples. This might be a problem when analyzing complex environmental samples of previously unknown composition. In such cases the combination of STXM with other techniques such as bulk chemical analysis might be useful to minimize systematic errors. However, in this study we used a cyanobacterial culture grown under well-defined conditions and we could additionally refer to an extensive spectral characterization of a large number of similarly prepared samples (Obst *et al.*, 2009a) which reduces the risk of selecting inappropriate reference spectra for the spectral deconvolution. However, even for relatively complex environmental river biofilm samples, the systematic error caused by differences of the actual spectra and those of reasonably appropriate reference compounds was estimated to be no more than a factor of two (Dynes *et al.*, 2006b). Clearly, OD image difference maps are less specific compared with a full spectral characterization. Therefore, inter- and intracellular variations in the organo-chemical composition of the cyanobacteria can result in similar absorption changes at specific energies to those caused by variations in thickness at a constant organo-chemical composition. However, the absorption at 288.2 eV is dominated by the two major components protein and lipids. The precise error of this method varies for each individual sample and cannot be easily quantified. Another potential artefact that has to be consid-

ered, particularly for image difference maps of species that have very sharp and intense absorption resonance peaks such as Ca-2p, is absorption saturation which can result in strong spectral distortions. For example, the ratio of the main absorption peak of aragonite at 352.6 eV to the absorption peak at 351.4 eV was increased from  $\sim 0.5$  to  $\sim 0.9$  due to saturation in thicker samples (Hanhan *et al.*, 2009). In the average Ca-2p spectrum of the cell presented in Fig. 2, which represents approximately a 1 : 1 ratio of aragonite-like  $\text{CaCO}_3$  and Ca adsorbed to EPS, a ratio of  $\sim 0.3$  was measured. Thus, artefacts from absorption saturation are not expected, although the OD difference from the Ca-2p pre-edge to the main absorption peak was as high as 1.2 in this particular data set. When the method of image difference mapping is combined with additional information about the sample such as a full spectral fit, we estimate the accuracy to be within a factor of two.

Another potential source of errors that should be considered is the geometry of angle-scan tomography samples. Because of the thickness of the TEM grid bars, the sample could not be scanned over the optimum range of  $\pm 90^\circ$  against the plane perpendicular to the X-ray beam but only  $\pm 70^\circ$ . The resulting ‘missing wedge’ (Kawase *et al.*, 2007) leads to artefacts in the reconstruction which affect both the shape of the reconstructed objects as well as the background intensity in the 3D data set. The first of these artefacts was modelled to be an elongation parallel to the incident beam axis in the range of 5%, and measured to be in the range of approximately 10% in a transmission electron microtomography study of zirconia grains in a polymer nanocomposite (Kawase *et al.*, 2007). Although the imaging techniques are not directly comparable, the artefacts are expected to be in the same range as they mostly derive from the 3D reconstruction of angle-scan data sets over limited angular ranges. In our experiment, this overestimation in the *Z*-dimension, respectively, leads to an underestimation of the species concentration in the volume data set by a similar value (5–10%).

The second reconstruction artefact is background, which makes it challenging to reconstruct and render signals at very low concentrations. Therefore, we used a threshold value which sets the lower limit of the concentrations used for quantitative analysis. Assuming a composition of 100% protein and 100% adsorbed  $\text{Ca}^{2+}$ , the threshold OD levels used – 0.031 per voxel for organic carbon and 0.012 per voxel for Ca – are equivalent to concentrations of  $2.8 \times 10^{-18}$  g per voxel ( $20 \times 20 \times 20 \text{ nm}^3$ ) for the organic carbon and  $2.4 \times 10^{-19}$  g per voxel ( $20 \times 20 \times 20 \text{ nm}^3$ ) for the adsorbed  $\text{Ca}^{2+}$  respectively. These limits are dependent on the quality of the individual data set, the geometry of the sample, the angle step size and the reconstruction algorithm used. The threshold limits could potentially be reduced further if time and radiation damage limitations allow for recording data sets with smaller angle steps than the  $5^\circ$  steps used in this work.

## CONCLUSIONS

The 3D distribution of the organic carbon and Ca content of a cell-mineral aggregate was analyzed quantitatively at sub-100-nm spatial resolution. Previous interpretations from 2D projection studies were verified by these 3D measurements, in particular, the relatively lower cell-internal sorption of Ca and the co-localization of EPS with both an adsorbed Ca species and an aragonite-like CaCO<sub>3</sub> layer.

In this study we have shown that STXM spectro-tomography is a very powerful technique for the quantitative 3D analysis of geomicrobiological samples at sub-100-nm resolution. The combination of 3D chemically sensitive mapping with 2D spectromicroscopy for precise spectral fitting of the components allows for a full 3D characterization of the distribution and detailed co-localization analysis of the relevant species. As an important future perspective, this approach offers the possibilities of quantitative high-resolution analysis of chemical properties such as metal sorption capacities of intra- and extracellular biomacromolecules and cell compartments.

## ACKNOWLEDGEMENTS

We thank J.J. Dynes, G.D.W. Swerhone, J.R. Lawrence (Environment Canada) for their support with the cell culture and precipitation experiments. We also thank Göran Johansson for excellent contributions to initial establishment of STXM tomography; David Kilcoyne and Tolek Tyliczszak for providing essential support for the STXM instruments at the 5.3.2 and 11.0.2 beamlines at the Advanced Light Source (ALS). Research is supported by NSERC, Canadian Foundation for Innovation, and the Canada Research Chair program. The ALS is supported by the Office of Basic Energy Sciences of the US Department of Energy.

## REFERENCES

- Abramoff MD, Viergever MA (2002) Computation and visualization of three-dimensional soft tissue motion in the orbit. *IEEE Transactions on Medical Imaging* **21**, 296–304.
- Attwood D (2000) *Soft X-rays and Extreme Ultraviolet Radiation: Principles and Applications*. Cambridge University Press, Edinburgh, New York, Oakleigh, Madrid, 470 pp.
- Benzerara K, Menguy N, Guyot F, Skouri F, de Luca G, Barakat M, Heulin T (2004a) Biologically controlled precipitation of calcium phosphate by *Ramlibacter tataouinensis*. *Earth and Planetary Science Letters* **228**, 439–449.
- Benzerara K, Yoon TH, Tyliczszak T, Constantz B, Spormann AM, Brown GE (2004b) Scanning transmission X-ray microscopy study of microbial calcification. *Geobiology* **2**, 249–259.
- Benzerara K, Menguy N, Guyot F, Vanni C, Gillet P (2005) TEM study of a silicate-carbonate-microbe interface prepared by focused ion beam milling. *Geochimica et Cosmochimica Acta* **69**, 1413–1422.
- Benzerara K, Morin G, Yoon TH, Miot J, Tyliczszak T, Casiot C, Bruneel O, Farges F, Brown GE (2008) Nanoscale study of As biomineralization in an acid mine drainage system. *Geochimica et Cosmochimica Acta* **72**, 3949–3963.
- Bluhm H, Andersson K, Araki T, Benzerara K, Brown GE, Dynes JJ, Ghosal S, Gilles MK, Hansen HC, Hemminger JC, Hitchcock AP, Kettler G, Kilcoyne ALD, Kneedler E, Lawrence JR, Leppard GG, Majzlam J, Mun BS, Myneni SCB, Nilsson A, Ogasawara H, Ogle-tree DF, Pecher K, Salmeron M, Shuh DK, Tonner B, Tyliczszak T, Warwick T, Yoon TH (2006) Soft X-ray microscopy and spectroscopy at the molecular environmental science beamline at the advanced light source. *Journal of Electron Spectroscopy and Related Phenomena* **150**, 86–104.
- Daulton TL, Little BJ, Lowe K, Jones-Meehan J (2001) In situ environmental cell-transmission electron microscopy study of microbial reduction of chromium(VI) using electron energy loss spectroscopy. *Microscopy and Microanalysis* **7**, 470–485.
- De Yoreo JJ, Vekilov PG (2003) Principles of crystal nucleation and growth. In *Biomineralization* (eds Dove PM, De Yoreo JJ, Weiner S). Mineralogical Society of America, Washington, DC, pp. 57–93.
- Dynes JJ, Lawrence JR, Korber DR, Swerhone GDW, Leppard GG, Hitchcock AP (2006a) Quantitative mapping of chlorhexidine in natural river biofilms. *Science of the Total Environment* **369**, 369–383.
- Dynes JJ, Tyliczszak T, Araki T, Lawrence JR, Swerhone GDW, Leppard GG, Hitchcock AP (2006b) Speciation and quantitative mapping of metal species in microbial biofilms using scanning transmission X-ray microscopy. *Environmental Science and Technology* **40**, 1556–1565.
- Gilbert P (1972) Iterative methods for 3-dimensional reconstruction of an object from projections. *Journal of Theoretical Biology* **36**, 105–117.
- Graham LL, Beveridge TJ (1994) Structural differentiation of the *Bacillus subtilis*-168 cell-wall. *Journal of Bacteriology* **176**, 1413–1421.
- Hanhan S, Smith AM, Obst M, Hitchcock AP (2009) Optimization of analysis of soft X-ray spectromicroscopy at the Ca 2p edge. *Journal of Electron Spectroscopy and Related Phenomena* **173**, 44–49.
- Herman GT, Lent A, Rowland SW (1973) ART – Mathematics and applications – Report on mathematical foundations and on applicability to real data of algebraic reconstruction techniques. *Journal of Theoretical Biology* **42**, 1–32.
- Hitchcock AP (2008) aXis2000 is written in Interactive Data Language (IDL). It is available free for non-commercial use from <http://unicorn.mcmaster.ca/aXis2000.html>.
- Hitchcock AP, Dynes JJ, Johansson G, Wang J, Botton G (2008) Comparison of NEXAFS microscopy and TEM-EELS for studies of soft matter. *Micron* **39**, 311–319.
- Hunter RC, Hitchcock AP, Dynes JJ, Obst M, Beveridge TJ (2008) Mapping the speciation of iron minerals in *Pseudomonas aeruginosa* biofilms using scanning transmission x-ray microscopy. *Environmental Science and Technology* **42**, 8766–8772.
- Ingraham JL, Maaloe O, Neidhardt FC (1983) *Growth of the Bacterial Cell*. Sinauer Associates, Sunderland, MA.
- Johansson GA, Tyliczszak T, Mitchell GE, Keefe MH, Hitchcock AP (2007) Three-dimensional chemical mapping by scanning transmission X-ray spectromicroscopy. *Journal of Synchrotron Radiation* **14**, 395–402.
- Kawase N, Kato M, Nishioka H, Jinnai H (2007) Transmission electron microtomography without the “missing wedge” for quantitative structural analysis. *Ultramicroscopy* **107**, 8–15.
- Kilcoyne ALD, Tyliczszak T, Steele WF, Fakra S, Hitchcock P, Franck K, Anderson E, Harteneck B, Rightor EG, Mitchell

- GE, Hitchcock AP, Yang L, Warwick T, Ade H (2003) Interferometer-controlled scanning transmission X-ray microscopes at the advanced light source. *Journal of Synchrotron Radiation* **10**, 125–136.
- Konhauser KO (1997) Bacterial iron biomineralisation in nature. *Fems Microbiology Reviews* **20**, 315–326.
- Konhauser KO (1998) Diversity of bacterial iron mineralization. *Earth-Science Reviews* **43**, 91–121.
- Koprinarov IN, Hitchcock AP, McCrory CT, Childs RF (2002) Quantitative mapping of structured polymeric systems using singular value decomposition analysis of soft X-ray images. *Journal of Physical Chemistry B* **106**, 5358–5364.
- Lawrence JR, Swerhone GDW, Leppard GG, Araki T, Zhang X, West MM, Hitchcock AP (2003) Scanning transmission X-ray, laser scanning, and transmission electron microscopy mapping of the exopolymeric matrix of microbial biofilms. *Applied and Environmental Microbiology* **69**, 5543–5554.
- Lerotic M, Jacobsen C, Schafer T, Vogt S (2004) Cluster analysis of soft X-ray spectromicroscopy data. *Ultramicroscopy* **100**, 35–57.
- Merz-Preiss M (2000) Calcification in cyanobacteria. In *Microbial Sediments* (eds Riding RE, Awramik SM). Springer-Verlag/Heidelberg, Berlin/New York, pp. 50–56.
- Messaoudil C, Boudier T, Sorzano COS, Marco S (2007) TOMOJ: tomography software for three-dimensional reconstruction in transmission electron microscopy. *BMC Bioinformatics* **8**, 9.
- Midgley PA, Weyland M (2003) 3D electron microscopy in the physical sciences: the development of Z-contrast and EFTEM tomography. *Ultramicroscopy* **96**, 413–431.
- Miot J, Benzerara K, Morin G, Kappler A, Bernard S, Obst M, Férard C, Skouri-Panet F, Guigner J-M, Posth N, Galvez M, Brown GE Jr, Guyot F (2009) Iron biomineralization by anaerobic neutrophilic iron-oxidizing bacteria. *Geochimica et Cosmochimica Acta* **73**, 696–711.
- Obst M, Dynes JJ, Lawrence JR, Swerhone GDW, Benzerara K, Karunakaran C, Kaznacheev K, Tyliczcak T, Hitchcock AP (2009a) Precipitation of amorphous CaCO<sub>3</sub> (aragonite-like) by cyanobacteria: a STXM study of the influence of EPS on the nucleation process. *Geochimica et Cosmochimica Acta* **73**, 4180–4198.
- Obst M, Wehrli B, Dittrich M (2009b) CaCO<sub>3</sub> nucleation by cyanobacteria: laboratory evidence for a passive, surface-induced mechanism. *Geobiology* **7**, 324–347.
- Phoenix VR, Adams DG, Konhauser KO (2000) Cyanobacterial viability during hydrothermal biomineralisation. *Chemical Geology* **169**, 329–338.
- Ress DB, Harlow ML, Marshall RM, McMahan UJ (2004) Methods for generating high-resolution structural models from electron microscope tomography data. *Structure* **12**, 1763–1774.
- Rightor EG, Hitchcock AP, Ade H, Leapman RD, Urquhart SG, Smith AP, Mitchell GE, Fischer D, Shin HJ, Warwick T (1997) Spectromicroscopy of poly(ethylene terephthalate): comparison of spectra and radiation damage rates in X-ray absorption and electron energy loss. *Journal of Physical Chemistry B* **101**, 1950–1961.
- Schadler S, Burkhardt C, Kappler A (2008) Evaluation of electron microscopic sample preparation methods and imaging techniques for characterization of cell-mineral aggregates. *Geomicrobiology Journal* **25**, 228–239.
- Schultze-Lam S, Beveridge TJ (1994) Nucleation of celestite and strontianite on a cyanobacterial s-layer. *Applied and Environmental Microbiology* **60**, 447–453.
- Schultze-Lam S, Harauz G, Beveridge TJ (1992) Participation of a cyanobacterial-S layer in fine-grain mineral formation. *Journal of Bacteriology* **174**, 7971–7981.
- Sonnenfeld EM, Beveridge TJ, Doyle RJ (1985) Discontinuity of charge on cell-wall poles of *Bacillus subtilis*. *Canadian Journal of Microbiology* **31**, 875–877.
- Thompson JB, Schultze-Lam S, Beveridge TJ, DesMarais DJ (1997) Whiting events: biogenic origin due to the photosynthetic activity of cyanobacterial picoplankton. *Limnology and Oceanography* **42**, 133–141.
- Umeda H, Aiba H, Mizuno T (1996) somA, a novel gene that encodes a major outer-membrane protein of *Synechococcus* sp. PCC 7942. *Microbiology* **142**, 2121–2128.

## SUPPORTING INFORMATION

Additional Supporting Information may be found in the online version of this article:

**Fig. S1** (A) Rotation series of the 'biology' maps (OD<sub>288.2eV</sub>–OD<sub>282.0eV</sub>) from –65° to +70° in 5° steps; (B) rotation series of the Ca maps (OD<sub>352.6eV</sub>–OD<sub>350.3eV</sub>) from –65° to +70° in 5° steps. These series were used for a 3D reconstruction of the volume of the cell.

Please note: Wiley-Blackwell are not responsible for the content or functionality of any supporting materials supplied by the authors. Any queries (other than missing material) should be directed to the corresponding author for the article.